Research Article

Enhanced dye degradation capability and reusability of Fe-based amorphous ribbons by surface activation

Fang Miao [a], Qianqian Wang [a,*], Siyi Di [a], Lu Yun [a], Jing Zhou [a], Baolong Shen [a,b,**]

[a] School of Materials Science and Engineering, Jiangsu Key Laboratory for Advanced Metallic Materials, Southeast University, Nanjing 211189, China
[b] Institute of Massive Amorphous Metal Science, China University of Mining and Technology, Xuzhou 221116, China

ABSTRACT

The dye degradation capability and reusability of FeSiBNbCu amorphous ribbons are largely enhanced due to the surface activation by ball milling. The time required for degrading 50 % of acid orange 7 solution by the activated FeSiBNbCu amorphous ribbons is only 1/6 of that by the as-quenched ribbons, while the reusable times of the activated ribbons is 6 times larger than that of the as-quenched ribbons. The superior degradation capability and better reusability of the activated FeSiBNbCu amorphous ribbons come from not only the uneven topography of the ribbon surface induced by ball milling, but also the stored deformation energy, including the structural rejuvenation and the enlarged residual stress. The structural rejuvenation in the activated FeSiBNbCu amorphous ribbons is verified by heat relaxation analysis, and the increased residual stress is confirmed by the magnetic domain measurements on the ribbon surfaces. Besides, the environmental adaptability of the activated FeSiBNbCu amorphous ribbons is also investigated. The possible pathways for degradation of acid orange 7 using the activated ribbons, including azo bond cleavage and hydroxylation of benzene ring, are proposed. This work provides a new method to effectively improve the degradation performance of amorphous ribbons.

© 2020 Published by Elsevier Ltd on behalf of The editorial office of Journal of Materials Science & Technology.

1. Introduction

Fe-based amorphous alloys have been widely studied because of their excellent magnetic, mechanical, and chemical properties [1–3], and have been produced on an industrial scale, providing a mature and stable market [4]. Recently, Fe-based amorphous alloys are reported to show high efficiency in degrading organic contaminants in wastewater, especially azo dyes, owing to their metastable nature and large density of active sites [5–11]. The dye degradation efficiency of Fe-based amorphous alloys varies substantially with their compositions. For example, the large atomic size of yttrium in $Fe_{76}Si_{12}B_9Y_3$ amorphous alloy induced heterogeneous structure consisting of Fe-rich and Fe-poor regions to form galvanic cells, which tremendously improved the degradation efficiency of the alloy [12]. $Fe_{80}P_{13}C_7$ amorphous ribbons exhibited a higher degra-

dation efficiency than $Fe_{78}Si_9B_{13}$ amorphous ribbons due to the galvanic cells formed between the strong Fe-C and the weak Fe-P bonds [6].

Other than modifying the compositions of Fe-based amorphous ribbons, two methods are usually adopted to improve their degradation ability, i.e., ball milling the ribbons into powders or annealing to prepare multi-phase nanocrystalline ribbons. The ball-milled powders have a large specific surface area and thus have excellent degradation efficiency. For instance, Wang et al. reported that the ball-milled $Fe_{73}Si_7B_{17}Nb_3$ amorphous powders with rough surfaces showed much higher efficiency in degrading the direct blue 6 than the gas-atomized $Fe_{73}Si_7B_{17}Nb_3$ amorphous powders that have smooth surfaces [13]. Xie et al. reported that the ball-milled $Fe_{76}B_{12}Si_9Y_3$ amorphous powders had extraordinary degradation efficiency towards methyl orange [12]. However, recycling of the powders is difficult and storage is challenging due to the oxidation in air. For multi-phase nanocrystalline ribbons, galvanic cells can form between different phases to improve the electron donation rate, thus promoting the dye degradation efficiency [14]. Chen et al. found that the annealed $(Fe_{73.5}Si_{13.5}B_9Nb_3Cu_1)_{91.5}Ni_{8.5}$ amorphous ribbons showed high degradation capabilities for orange II and methyl orange due to the formation of galvanic cells between the α-Fe nanocrystals

---

and the intermetallics [15]. Rejuvenation of the catalytic ability of $Fe_{73.5}Si_{13.5}B_9Cu_1Nb_3$ amorphous ribbons has been achieved in the multi-phase crystalline ribbons after annealing [16]. However, the annealing treatment is an energy-consuming process due to the high annealing temperatures (773—1023 K) and high vacuum [15,16]. Therefore, it becomes critical to develop an efficient method to improve the degradation capability of amorphous ribbons.

It is known that the large residual stress and metastable nature of amorphous ribbons are the origins of their excellent degradation capabilities [17,18]. Chen et al. demonstrated that inhomogeneous residual stresses contributed to the high degradation capability due to the generated stress gradient cells and increased amount of active sites [19]. Thus, improving the residual stress can potentially enhance the dye degradation capability of Fe-based amorphous alloys [18,19]. It has been reported that plastic deformation can not only increase the residual stress [19–22], but also expand the interatomic distances to obtain high deformation energy [23,24]. Ball milling is an effective method to induce plastic deformation. Besides, the ball milling process can produce many corrugations on the ribbon surfaces, which have been confirmed to be beneficial to a high degradation efficiency toward azo dyes [13]. Based on the above discussion, the ball milling treatment (without grinding the ribbons into pieces) is an effective surface activating method to improve the dye degradation efficiency of Fe-based amorphous ribbons.

FeSiBNbCu amorphous ribbons, which are produced in a large scale in industry because of their excellent soft magnetic properties, have been reported to show excellent capability to degrade organic contaminants in wastewater. For example, it was found that the $Fe_{73.5}Si_{13.5}B_9Nb_3Cu_1$ amorphous powders had a high efficiency in decreasing the concentration of the chemical oxygen demand (COD) in wastewater [25,26]. Jia et al. reported that $Fe_{73.5}Si_{13.5}B_9Nb_3Cu_1$ ribbons exhibited an advanced catalytic capability in Fenton-like reactions to degrade methyl blue and methyl orange dyes [27].

Thus, in this work, we investigated the effects of ball milling treatment (without grinding the ribbons into pieces) on the dye degradation efficiency of $Fe_{73.5}Si_{15.5}B_7Nb_3Cu_1$ amorphous ribbons. It was demonstrated that $Fe_{73.5}Si_{15.5}B_7Nb_3Cu_1$ amorphous ribbons activated by ball milling have a far higher degradation efficiency and better reusability than the as-quenched amorphous ribbons. The superior degradation capability and better reusability of the activated ribbons came from the stored deformation energy and the uneven topography of the ribbon surface induced by ball milling. In addition, the effects of temperature, initial pH, dye concentration, and initial ribbon dosage on the degradation efficiency of acid orange 7 (AO7) by the activated ribbons were studied. Finally, the degradation pathways of AO7 using the activated ribbons were also proposed. This work provides a new method to improve the dye degradation capability and reusability of amorphous ribbons.

2. Materials and methods

2.1. Materials

The FeSiBNbCu amorphous ribbons with a nominal composition of $Fe_{73.5}Si_{15.5}B_7Nb_3Cu_1$ (in atomic percentage) were prepared by induction melting of high-purity Fe, Si, B, Nb, and Cu (99.5—99.9 wt%). Ribbons with a width of approximately 7 mm and a thickness of 23 μm were prepared by melt spinning in the air. The azo dye AO7 ($C_{16}H_{11}N_2NaO_4S$, AR grade) was purchased from Xiya Reagent. Sodium hydroxide (NaOH, AR grade) was purchased from Greagent. Sulphuric acid (H_2SO_4, AR grade) was supplied by Chron Chemicals. The as-quenched FeSiBNbCu amorphous ribbons were cut into

approximately 1.5 cm long for degradation experiments (named AQ ribbons), and some ribbons were ball milled for 4 h at a speed of 350 revolutions per minute (rpm) under the protection of high-purity argon (named BM ribbons).

2.2. Chemical tests

For all the degradation experiments, 250 mL AO7 solution was prepared using deionized (DI) water in a 500 mL beaker. The initial pH of the solution was adjusted with 5% H_2SO_4 and 1 mol/L NaOH. The temperature of the solution was maintained using a water bath. A specific amount of ribbons were added into the solution, which were then mechanically stirred at a fixed speed. At selected time intervals, 3 mL of the solution was extracted using a syringe and filtered with a 0.22 μm membrane and then measured using a UV–vis spectrophotometer (Shimadzu UV-1280) to obtain the relative concentration of AO7 in the solution. For cyclic tests, the ribbons after each degradation experiment were first extracted from the solution and then sonicated in distilled water for 180 s before the next cycle. The electrochemical tests were carried out in a simulated AO7 (20 mg/L) solution at pH = 3, using an electrochemical station (Gamry Interface 1000) in a three-electrode cell with platinum counter electrode and Ag/AgCl reference electrode.

The degradation products of AO7 were identified by direct injection using ultra high-performance liquid chromatography (UHPLC, Dinonex Ultimate 3000), which was performed using the mass spectrometer (MS, Thermo Scientific Q Exactive) equipped with an electrospray ionization (ESI) interface source. The MS analysis was set in the negative and positive ion scanning mode and its range was 50—400 m/z. The heated capillary was set to 573.15 K. The mobile phase was a mixture of A phase (0.1 % formic acid, 99.9 % H_2O) and B phase ($C_7H_6N_2$), and its gradient elution at A/B: 95/5 (v/v) by stepwise change.

2.3. Characterization

The amorphous nature of the ribbons was verified by X-ray diffraction (XRD, Bruker D8 Advance) with CuK_α radiation. The thermal responses of the ribbons were obtained from differential scanning calorimetry (DSC, NETZSCH 404F3) measurements. Ribbons were heated at 40 K min^{-1} from room temperature to 1073 K, then cooled to room temperature at 40 K min^{-1}. A second heating cycle, using the same settings, was used as the baseline for subtraction from the first cycle. The surface morphology and composition of the ribbons were studied using a scanning electron microscope (SEM, FEI Sirion 200) combined with an energy dispersive X-ray spectroscope (EDS). The local magnetic domain configurations on the ribbon surface was measured by magnetic force microscopy (MFM) using an atomic force microscope (AFM, Asylum Research MFP-3D) equipped with a magnetic tip (Nanosensors, PPP-MFMR). The magnetic tip was kept at a lift height of 100 nm to avoid topographic artifacts.

3. Results and discussion

3.1. Structure of the ribbons

The amorphous nature of both the AQ and BM ribbons are confirmed by XRD analyses, as only a broad peak at around $2\theta = 40°–50°$ appears on each curve, as shown in Fig. 1. The insets of Fig. 1 are photographs of the AQ and BM ribbons. The AQ ribbons are almost flat, while the BM ribbons are curled. It is worth noting that the BM ribbons roll up toward their free surfaces, which may be closely related to the difference of residual stress between the wheel and free surfaces of the BM ribbons [28]. Details about the residual stress
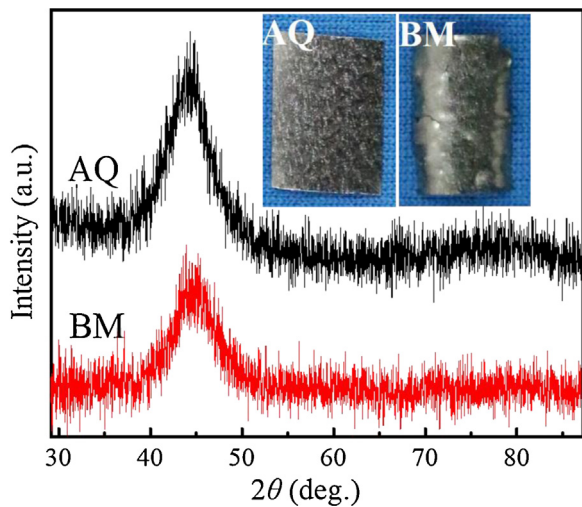
Fig. 1. XRD patterns of AQ and BM ribbons. Insets are the photographs of AQ and BM ribbons.

distribution of the ribbons before and after ball milling treatment will be discussed in Section 3.3.2 in this work.

3.2. Comparison of the degradation efficiency and reusability between AQ and BM ribbons

The degradation efficiency of AQ and BM ribbons toward AO7 solutions are compared via redox reactions, with the reaction parameters set as follows: temperature T =298 K, pH = 3, ribbon dosage =10 g/L, and initial AO7 concentration (C_{AO7}) = 20 mg/L. Fig. 2(a) and (b) shows the colour change of AO7 solutions with time when degraded using the AQ and BM ribbons, respectively. The solution is almost clear after it is degraded by the BM ribbons for 50 min. In contrast, the solution treated by the AQ ribbons is still yellowish even after 60 min.

Fig. 3(a) and (b) shows the UV–vis absorbance spectra of the filtered AO7 solutions after adding the AQ and BM ribbons, respectively. The maximum adsorption peak at 485 nm, arising from the azo chromophore of AO7, is proportional to the dye concentration in the solution. The intensity of the peak gradually decreases with the reaction time, indicating the breakage of the chromophore bonds [29]. The concentration of the AO7 solution using the BM ribbons decreases significantly within the first 5 min, while the reaction rate using the AQ ribbons is very slow at the same time. To compare the reaction efficiency quantitatively, the normalized concentration change is shown in Fig. 3(c). It is observed that the AO7 removal rate by the BM ribbons is much faster than that by the AQ ribbons. The degradation efficiency is measured at the time when the peak intensity becomes half of the initial peak intensity (t50 %). The t50 % of the AO7 solutions degraded by the BM ribbons is 5 min, much faster than that by the AQ ribbons (~30 min). These results demonstrate that the dye degradation efficiency of the BM ribbons is approximately 6 times faster than the AQ ribbons. The degradation curves are fitted with a pseudo-first-order kinetic model and then the corresponding reaction rate constant (k) is calculated according to the following equation:

$$\ln\left(\frac{C_0}{C_t}\right) = kt \tag{1}$$

where k is the reaction rate constant (min^{-1}), C_0 is the initial concentration, and C_t is the concentration at time t of the AO7 solution.

According to the ln (C_0/C_t) vs. time curves for the AQ and BM ribbons in Fig. 3(d), k for the AQ ribbons in this redox reaction is 0.015 min^{-1}, which is lower than that for the BM ribbons (0.021 min^{-1}).

In order to further understand the difference of AQ and BM ribbons in the reaction performance, the reaction activation energies using both ribbons are measured by carrying out the dye degradation experiments at different temperatures. As shown in Fig. S1 (Supporting Information), the reaction activation energy of the BM ribbons is 2.5 kJ/mol, and that of the AQ ribbons is 16.1 kJ/mol. The lower reaction activation energy of the BM ribbons contributes to its better performance in the redox reaction. Based on the above results, it is confirmed that the dye degradation efficiency of the FeSiBNbCu amorphous ribbons can be improved by ball milling treatment. In addition, while peroxides (hydrogen peroxide, persulfate, peroxymonosulfate etc.) are usually added in the azo dye degradation using the amorphous ribbons to generate the strong oxidizing radicals [31–34], the BM ribbons prepared in this work show high efficiency in degrading AO7 by its own oxidizing ability. Furthermore, in order to compare the dye degradation ability of amorphous alloys (without assistance of peroxides), the reaction activation energy (ΔE) of BM ribbons and other amorphous alloys are shown in Table S1 (Supporting Information). According to Table S1, the Fe$_{73.5}$Si$_{15.5}$B$_7$Nb$_3$Cu$_1$ amorphous ribbons activated by ball milling (this work) have a lower reaction activation energy with good performance in the redox reaction.

Reusability of materials is an important factor for wastewater remediation applications. The reusability of AQ and BM ribbons are compared by cyclic tests for degrading AO7 dyes under the conditions of T =298 K, pH = 3, ribbon dosage =10 g/L, and C_{AO7} = 20 mg/L, with the results shown in Fig. 4(a) and (c), respectively. The redox reactions using the AQ ribbons are capable of decomposing 70 % of the AO7 within 60 min in the first 2 cycles. The 3rd cycle shows a very slow degradation rate compared with the 2nd cycle. The corresponding surface morphology of the AQ ribbons before the 3rd reaction cycle is shown in Fig. 4(b). A passive film is formed on the surface, mainly composed of silica and niobium oxide, causing reduction in degradation performance [26]. The redox reactions using the BM ribbons are capable of decomposing 70 % of the AO7 within 60 min during the first 12 cycles, suggesting that the BM ribbons can be reused at least 12 times without losing obvious degradation efficiency. The 13th cycle shows a slow degradation rate, decomposing only 57 % of the AO7 within 60 min. Fig. 4(d) illustrates the corresponding surface morphology of the BM ribbons before the 13th reaction cycle. The likely reason for the obviously declined degradation performance after the 12th cycle is that passivation layers are formed on the ribbon surface during the degradation process. The reusability of the FeSiBNbCu amorphous alloy system is not intrinsically excellent, but an obvious improvement in the reusability of the FeSiBNbCu amorphous ribbons is achieved by ball milling treatment. For Fe-based amorphous ribbons with excellent reusability, such as FePC and FeBC amorphous ribbons [6,30], their ball-milled counterparts should show even larger cyclic numbers.

Besides, the effects of pH, AO7 concentration and ribbon dosage on the dye degradation efficiency of the BM ribbons are studied, as shown in Fig. S2 (Supporting information). It shows that the degradation efficiency of BM ribbons decreases with increasing pH, increasing AO7 concentration, or decreasing ribbon dosage.

3.3. Origin of the improved degradation efficiency and reusability by ball milling treatment

3.3.1. Deformation-induced structural changes

As metallic glasses are in metastable state, they can go through structural relaxation when heated toward T_g, or structural rejuvenation when treated by thermal cycling or deformation [35,36]. Changes in relative relaxation enthalpy (ΔH_{rel}), which is calculated from the area between the onset of relaxation to the glass transition of the heating DSC curve, have been used to describe the structural
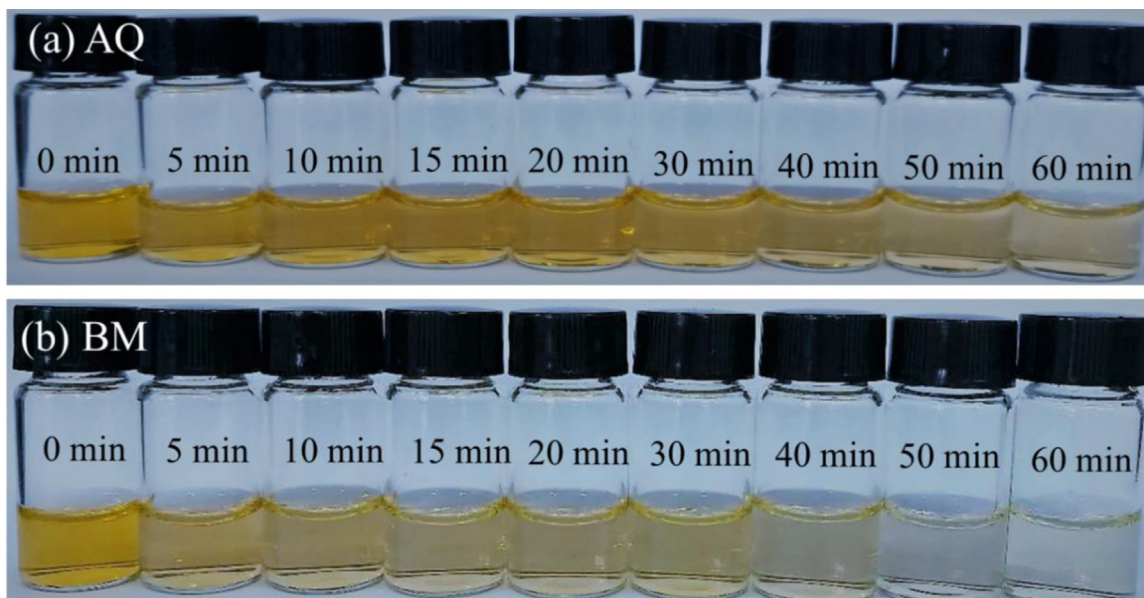
Fig. 2. Visible colour change of AO7 solution during redox reaction using (a) AQ and (b) BM ribbons.
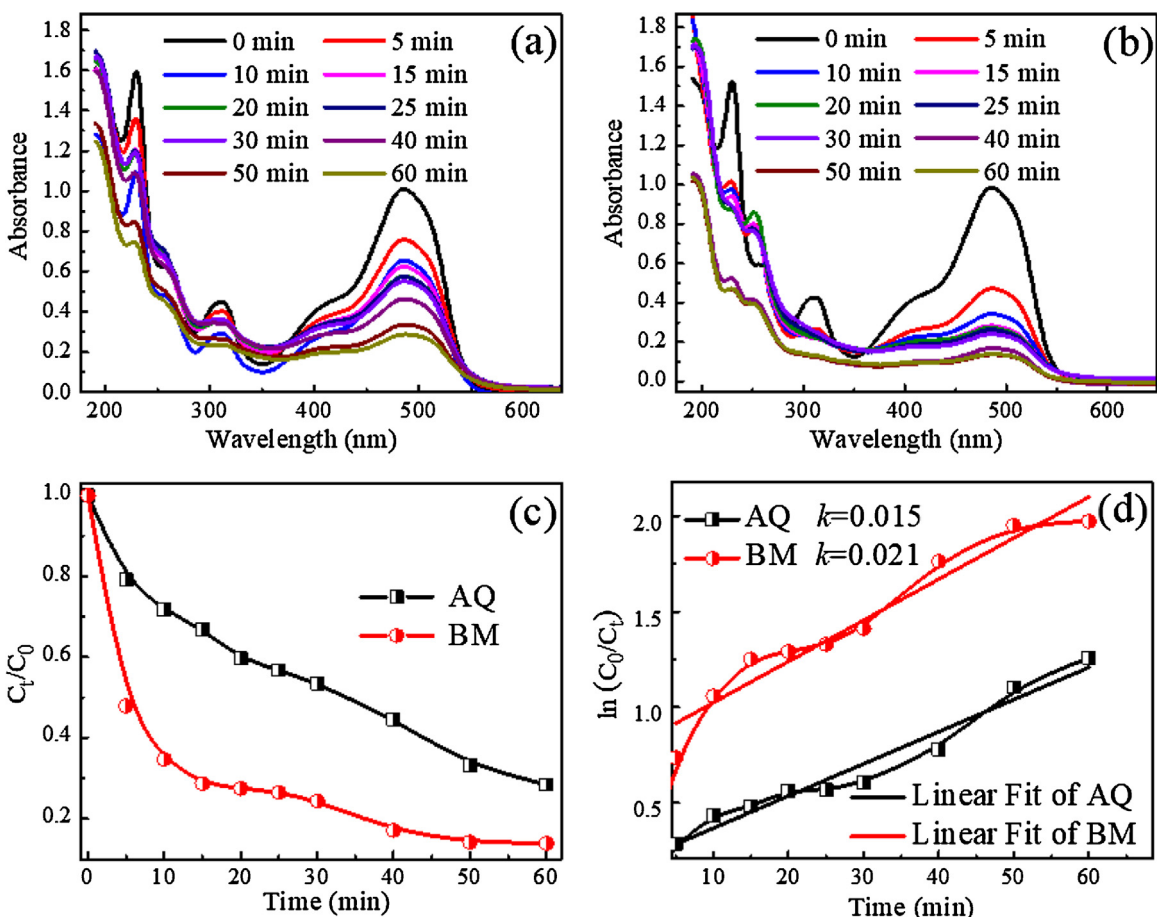

Fig. 3. UV–vis absorbance spectra of AO7 solutions during the redox reactions using (a) AQ and (b) BM ribbons; (c) normalized concentration change of AO7 solutions during the degradation process; (d) the ln (C_0/C_t) vs. time curves for AQ and BM ribbons (T = 298 K, pH = 3, ribbon dosage = 10 g/L, C_{AO7} = 20 mg/L).

changes of metallic glasses from thermal or mechanical treatments [20,37–39]. To gain insights into the structural change induced by the permanent deformation caused by ball milling treatment, ΔH_{rel} of the AQ and BM ribbons are compared. Fig. 5 displays the heating DSC curves of the AQ and BM ribbons obtained in ultrapure argon

gas. The glass transition temperature T_g for both samples are at 725 K, further confirming their amorphous nature. Both of the samples have two sets of strong exothermic peaks, indicating a two-step crystallization process [40]. The inset shows the magnified curves of the rectangular region in Fig. 5, showing an increase in ΔH_{rel}
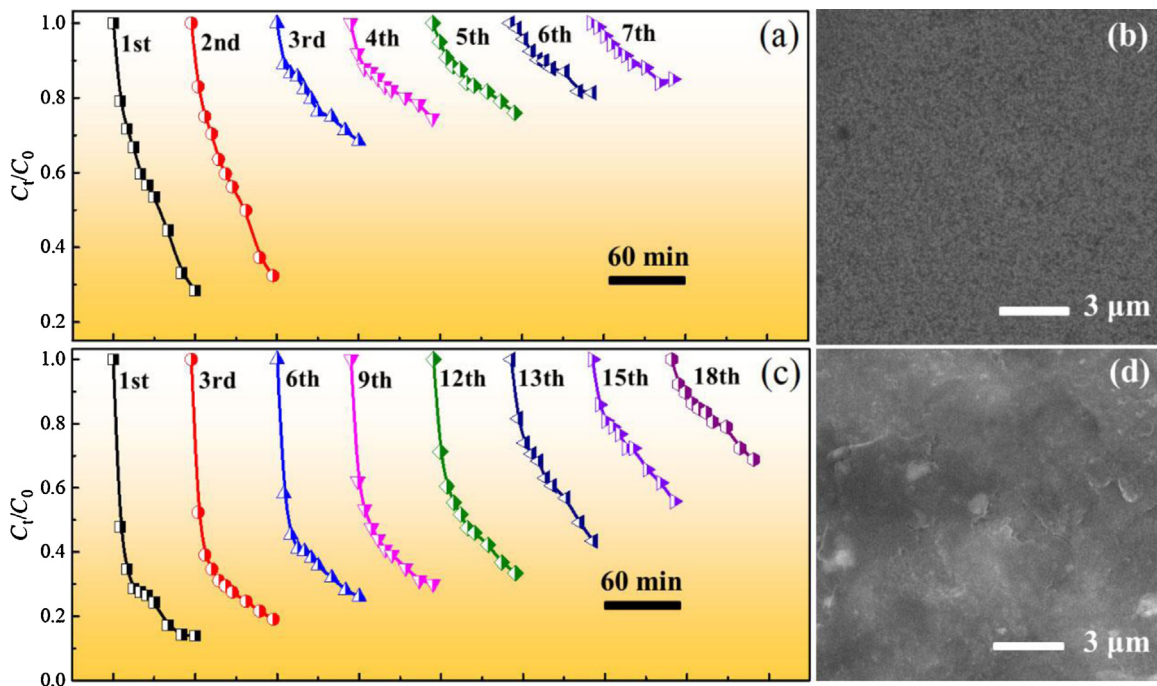
Fig. 4. Normalized concentration change of AO7 solutions at different degradation cycles during the redox reactions using (a) AQ ribbons and (c) BM ribbons; surface morphologies of (b) AQ ribbons after 2 degradation cycles and (d) BM ribbons after 12 degradation cycles.
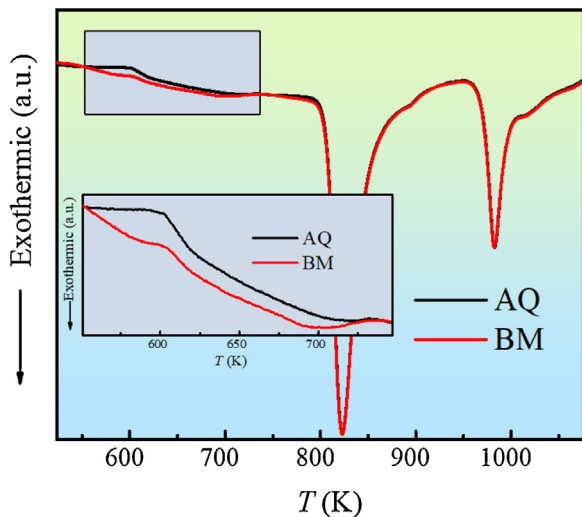

Fig. 5. DSC curves recorded for AQ and BM ribbons. The inset is the magnified view of the rectangular region.

after ball milling, which can be regarded as the stored energy of cold work [41]. The increased ΔH_{rel} implies structural rejuvenation of the FeSiBNbCu amorphous ribbons after ball milling, bringing them to higher-energy states. This explains the largely reduced reaction activation energy of the degradation using the BM ribbons, as well as the enhancement of the reaction rate and service life.

3.3.2. Large residual stress

Residual stress has been proved to have great impacts on the degradation efficiency of amorphous ribbons [17–19]. As the magnetic domain configurations can directly reflect the local stress distribution of a ferromagnetic amorphous alloy [42–45], the magnetic domain structures on the surface of the ribbons are measured by MFM to investigate the distribution of residual stress in the amorphous ribbons before and after ball milling. The regular zigzag

and planar domains, which are typical magnetic structures, are observed on both the free and wheel surfaces of the AQ ribbons, as shown in Fig. 6(a) and (b), respectively. Based on the Chikazumi and Suzuki formula, the square of the width of the magnetic domains is inversely proportional to the mean stress [28]. For AQ ribbon, as the width of both the zigzag and planar domains on the wheel surface is smaller than that on the free surface, it can be concluded that the total stress on the wheel surface is higher than that on its free side. Magnetic domains on the free and wheel surfaces of the BM ribbons are shown in Fig. 6(c) and (d), respectively. Only irregular and fine zigzag domain structure can be observed on the free and wheel surfaces of the BM ribbons. Compared with the AQ ribbons, the magnetic domains on the surface of the BM ribbons are finer, in another word, the width of the domains is much smaller after ball milling. More refined domain structure indicates greater residual stress [28,44]. It can be inferred that a larger stress is involved on the wheel and free surfaces of the BM ribbons than that of the AQ ribbons.

Furthermore, compared with the free surface of BM ribbons, the magnetic domains on the wheel surface of the BM ribbons are finer, indicating that the wheel surface has larger residual stress than free surface after ball milling. The ribbon surface with larger residual stress tends to appear on the convex side [28]. This explains why all BM ribbons roll up toward their free surfaces.

In addition, the height distributions of the AQ and BM ribbon surfaces derived from the AFM analyses are shown in Fig. 6(e) and (f), showing details of the profiles on the ribbon surfaces. The height distribution on the free surfaces of the AQ and BM ribbons ranges from -40 to 40 nm and -400 to 400 nm (Fig. 6(e)), respectively. The height distribution on the wheel surfaces of the AQ and BM ribbons ranges from −80 to 80 nm and −550 to 550 nm (Fig. 6(f)), respectively. The heights on the free and wheel surfaces of the BM ribbons are an order larger than those of the AQ ribbons. As a greater observed height indicates a larger residual stress involved on the surface [44], this result further confirms that a larger stress is produced on both the free and wheel surfaces of the BM ribbons. Besides, the maximum fraction on the height distribution curve for
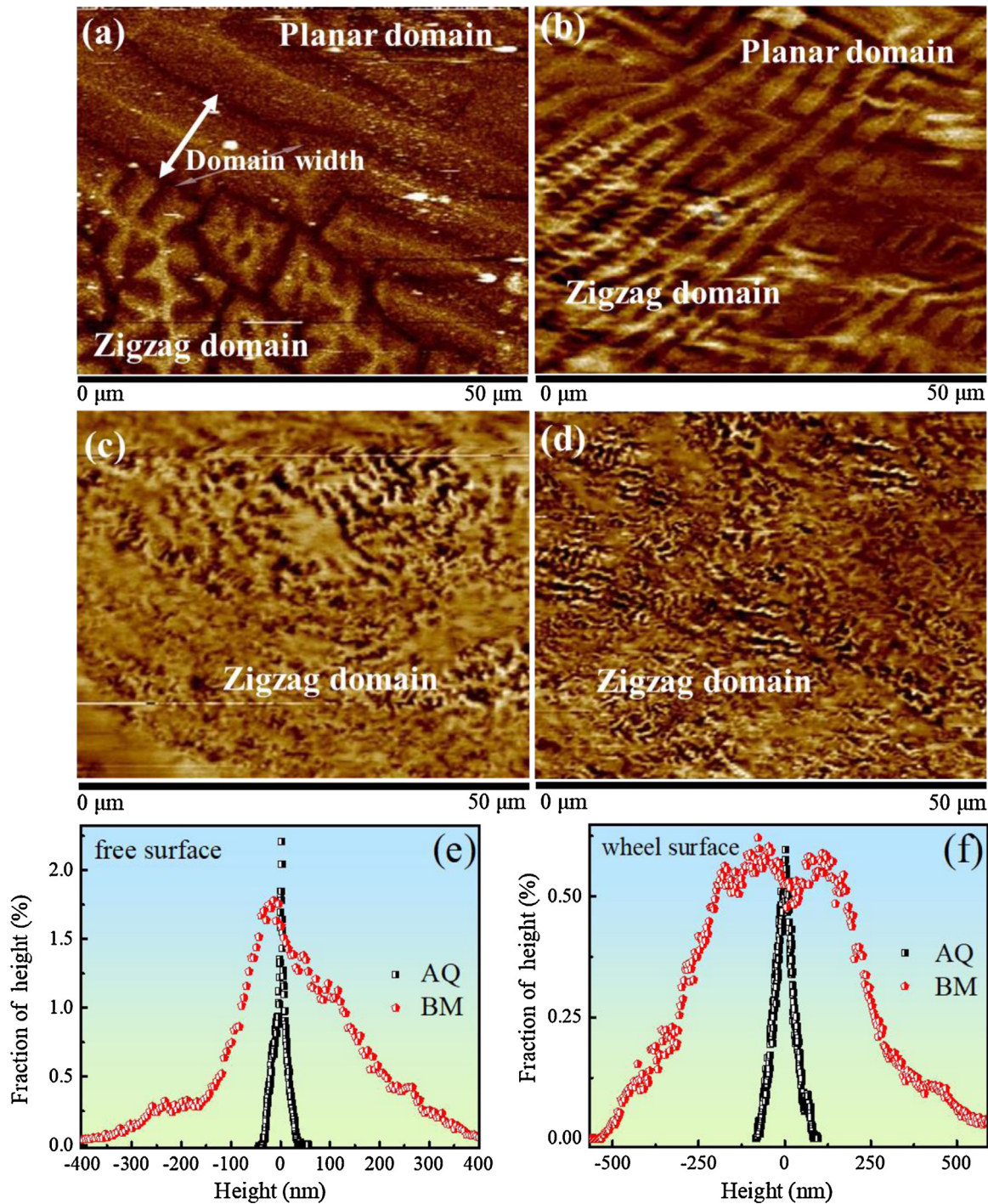
Fig. 6. MFM images of the magnetic structure on the (a) free and (b) wheel surfaces of AQ ribbons; MFM images of the magnetic structure on the (c) free and (d) wheel surfaces of BM ribbons. Height distributions on the (e) free surfaces of AQ and BM ribbons; height distributions on the (f) wheel surfaces of AQ and BM ribbons.

the wheel surface of BM ribbon deviates from 0 nm due to the large stress and surface roughness. Based on the above analyses, the ball milling treatment gives rise to residual stress on the ribbon surface, which contributes to the improved degradation performance and service life of BM ribbons [19].

3.3.3. Surface morphology

As degradation occurs on the surface, the surface morphologies and elemental information of AQ and BM ribbons before and after reactions, which have a significant influence on their degradation efficiency, are inspected by SEM and EDS. Before degradation, the surface morphology of the AQ ribbons is very smooth (Fig. 7(a)), while the surface of the BM ribbons is full of numerous protrusions and corrugations (Fig. 7(b)). A larger surface area is available on the rough surface to provide reaction sites, and thus accelerates the redox reaction to degrade AO7. As shown in Fig. 7(c), after degradation, a homogeneous passive film is formed on the surface of AQ ribbon, as the inclusion of Nb in the amorphous ribbons could enhance the surface stability and thus results in a lower reaction activity and shorter service life by forming insoluble niobium oxides [26,46]. In contrast, the surface of the reacted BM ribbons is covered by the newly generated 3D nanoporous structure, as shown
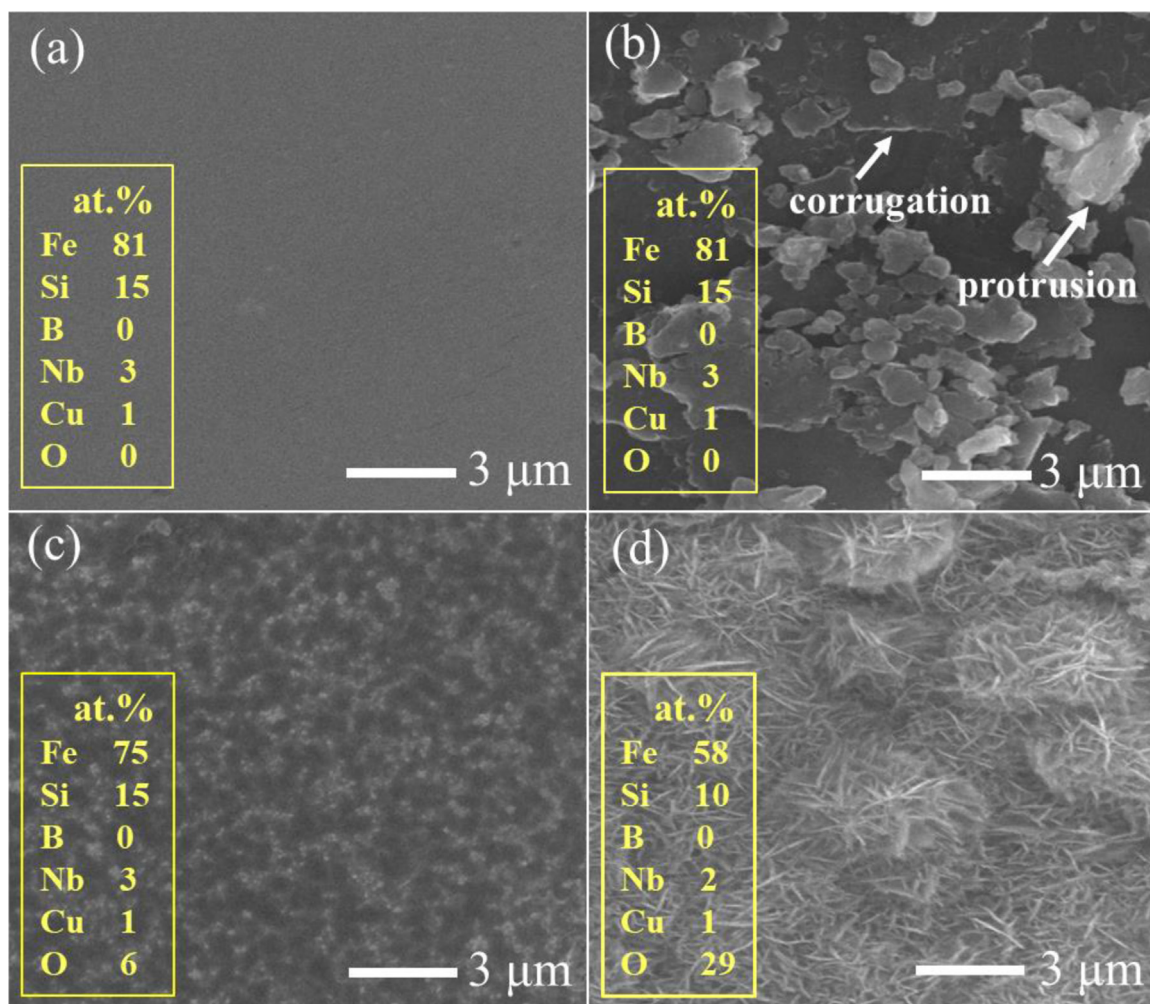
Fig. 7. SEM micrographs of AQ ribbons (a) before and (c) after reactions; SEM micrographs of BM ribbons (b) before and (d) after reactions. Insets show the compositions of corresponding samples obtained from EDS measurements.

in Fig. 7(d). The nanoporous structure may result from selective corrosion, such as galvanic corrosion coming from the stress gradient cells [19]. It has been reported that the nanoporous structure has positive effects on the decolorization process, as the high density of pores provide channels for mass transfer and a large amount of active sites for the redox reaction [47]. Therefore, the formed nanoporous structures during reaction on the surface of BM ribbons improves the degradation performance and service life.

The insets of the Fig. 7 show the EDS data on the surfaces of the AQ and BM ribbons before and after reaction. The amount of oxygen is too small to be detected on both unreacted ribbons but increases to 6 and 29 at.% for the reacted AQ and BM ribbons, respectively. The increase of oxygen indicates that both ribbons are involved in a redox reaction, but the BM ribbons participate more actively in the redox reaction than the AQ ribbons.

Besides, XPS analyses were carried out on the AQ and BM ribbons, as shown in Fig. S3 (Supporting Information), and the atomic valence or elemental contents of AQ and BM ribbons are almost the same, indicating that ball milling has not change the atomic valence and elemental contents of $Fe_{73.5}Si_{15.5}B_7Nb_3Cu_1$ amorphous ribbons.

3.3.4. Corrosion properties

As the corrosion resistance of the ribbons is critical to the decolorization applications, the corrosion properties of the AQ and BM ribbons are compared via electrochemical tests. Fig. 8(a) shows the electrochemical polarization dynamic curves of both ribbons in AO7 solutions (T = 298 K, pH = 3, and C_{AO7} = 20 mg/L), from which the corrosion potential density (E_0) and corrosion current density (I_{corr}) are obtained. E_0 of the BM ribbons is −0.42 V, which is lower than −0.39 V for the AQ ribbons. I_{corr} is 1.8×10^{-7} and 5.3×10^{-7} A cm^{-2} for the AQ and BM ribbons, respectively. The smaller E_0 and higher I_{corr} of the BM ribbons indicate a lower corrosion resistance, which is more beneficial to the degradation process in this work.

Nyquist plots are derived from the electrochemical impedance spectra (EIS) of the AQ and BM ribbons (Fig. 8(b)), where the frequency response of the electrode/electrolyte system is the relationship between the imaginary component (Z'') and the real component (Z') of the impedance. The Nyquist plots of the AQ ribbons are semi-circular in the high frequency range and inclined in a straight line in the low frequency region. The large semicircle for the AQ ribbons indicates a high interfacial charge transfer resistance [4,48–50]. The straight slope of the Nyquist plots shows that the Warburg resistance generated by the frequency dependence of ion diffusion in the electrolyte [48]. The projected length of Warburg resistance on the real axis characterizes the electrolyte ion diffusion process in electrode materials [49,51]. The larger Warburg region of the AQ ribbons shows they have a longer path length for ion diffusion, thus indicating a greater obstacle for ion movement [49–51]. In contrast, small semicircle is detected in the Nyquist plots of the BM ribbons at high frequencies, which indicates that the interface charge transfer resistance within the BM ribbons is significantly
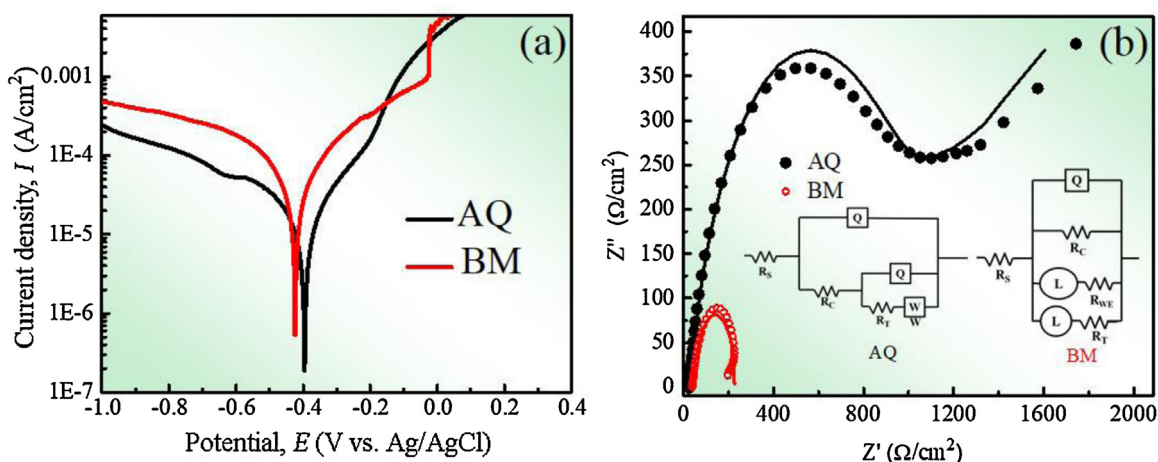
Fig. 8. (a) Polarization curves and (b) Nyquist plots derived from EIS measurements for AQ and BM ribbons in AO7 solutions, and the insets correspond to the equivalent circuits.
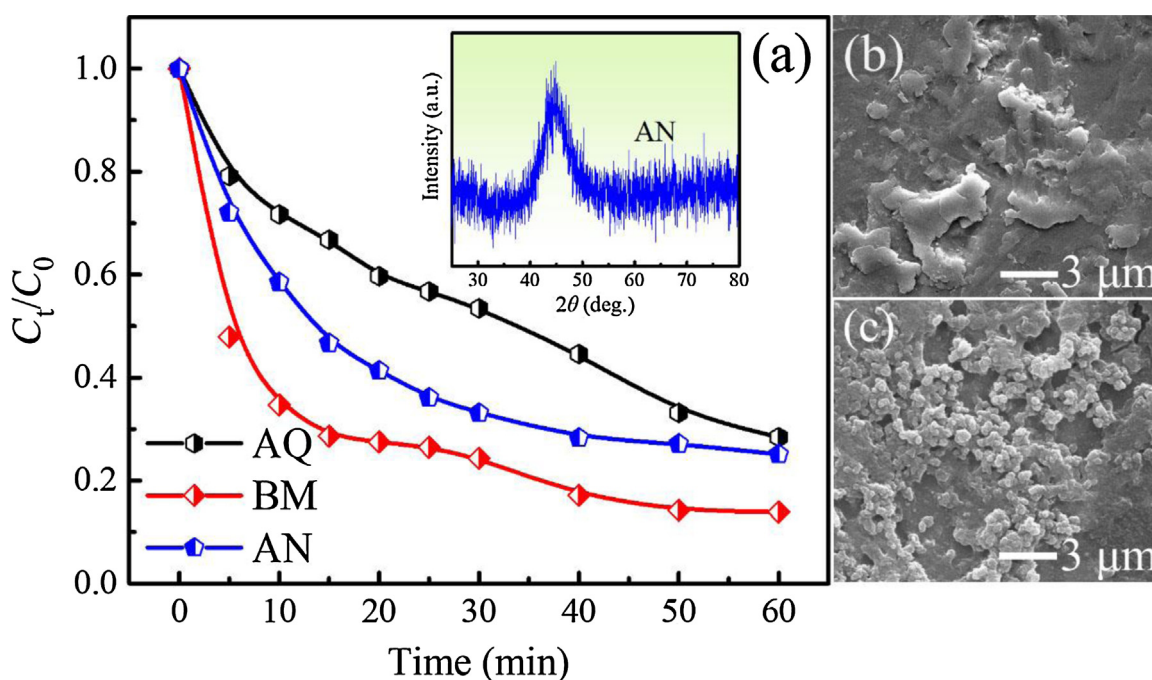

Fig. 9. (a) Normalized concentration change of AO7 solutions using AQ, BM and AN ribbons during the degradation process, the inset shows the XRD curve of AN ribbons; SEM micrographs of AN ribbons (b) before and (c) after reactions.

lower. The impedance data can be fitted with equivalent circuits, as seen in Fig. 8(b). In the equivalent circuits, Q, R_S, R_C, R_T, and R_{WE} represent the constant phase angle elements, solution resistance, polarization resistance, interfacial charge transfer resistance, and working electrode resistance, respectively. Generally, R_C is used to evaluate the corrosion resistance of electrode materials in electrolyte solution [52]. According to the fitted results, the R_C value of BM ribbon (361 Ω cm^2) is smaller than that of AQ ribbon (1047 Ω cm^2), indicating a lower corrosion resistance. Besides, the Q value is related to the surface roughness of electrode materials [53]. The Q value of BM ribbon (0.000184) is larger than that of AQ ribbon (0.000165), indicating the rougher surface of BM ribbon with more corrosion sites. The results from EIS analyses reveal that the BM ribbons have a lower corrosion resistance than the AQ ribbons in the AO7 solution.

The structural rejuvenation, large residual stress, and rough surface morphology generated by ball milling treatment contribute

to the low corrosion resistance of the BM ribbons. As the electron transfer ability on the surface of the BM ribbons is far stronger than that of the AQ ribbons, the BM ribbons have far better degradation efficiency and reusability than the AQ ribbons.

3.3.5. Annealing treatment to release deformation energy

To verify whether the stored deformation energy, including the structural rejuvenation and enlarged residual stress, contributes to the improvement of the degradation performance, the BM ribbons were treated by isothermal annealing at 663 K for 10 min (below T_g), allowing the structural relaxation and relief of the residual stress. The obtained ribbons are named as AN ribbons. The inset of the Fig. 9(a) shows the XRD pattern of the AN ribbons, confirming the amorphous nature of the AN ribbons. Fig. 9(a) shows the normalized concentration change of the AO7 solutions degraded by the AQ, BM, and AN ribbons, with the reaction parameters set as follows: T =298 K, pH = 3, ribbon dosage = 10 g/L, and C_{AO7} = 20
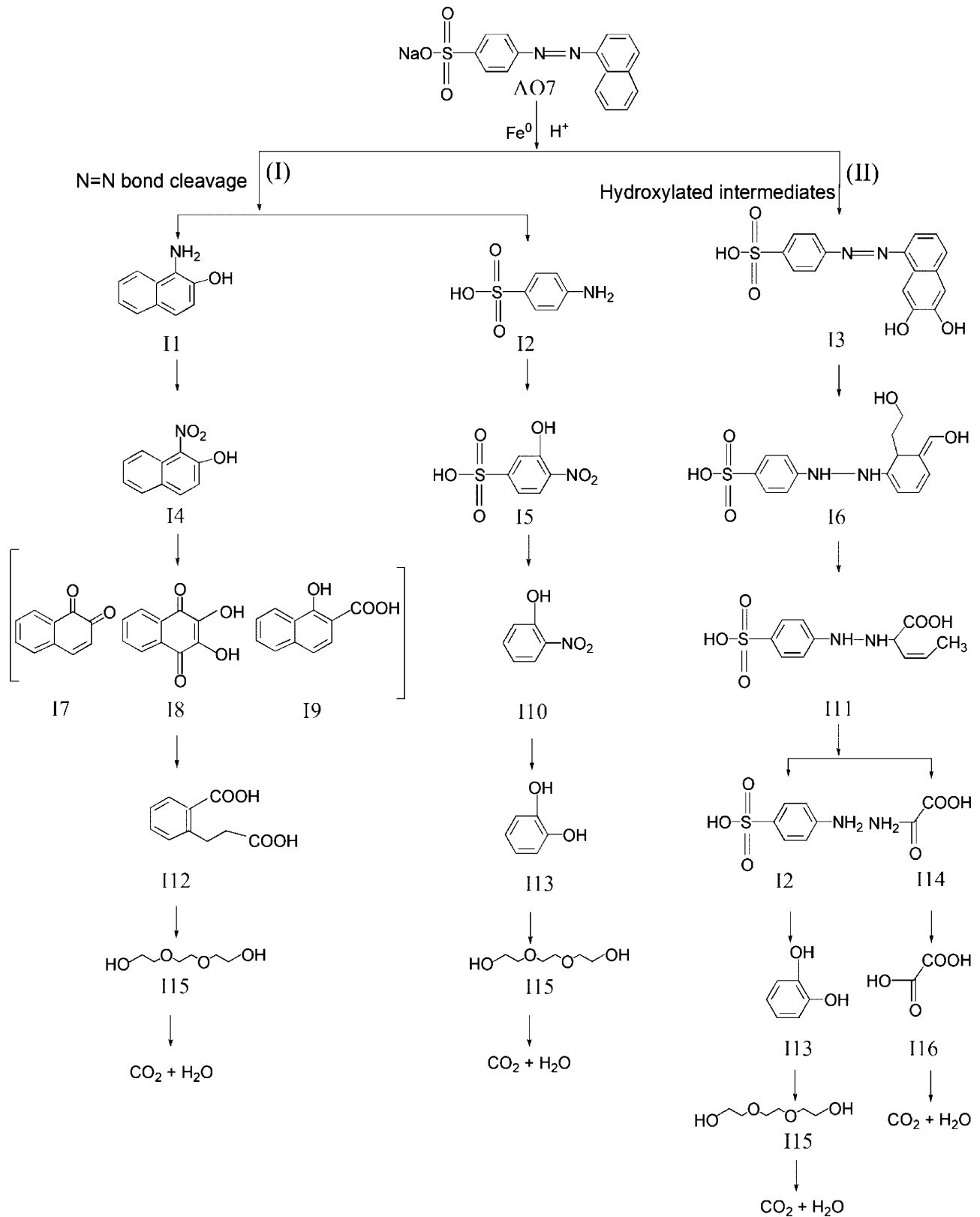
Fig. 10. Possible degradation pathways of AO7 during the redox reactions using BM ribbons.

mg/L. It is observed that the degradation efficiency of the AN ribbons is lower than that of the BM ribbons, but higher than that of the AQ ribbons.

In addition, many protrusions and corrugations can be seen on the surface of the AN ribbons before degradation (Fig. 9(b)), which is similar to the unreacted BM ribbons. The surface morphology of the reacted AN ribbons is presented in Fig. 9(c), showing a more concentrated reaction zone of protrusions and corrugations, which is different from that of the reacted AQ ribbons (passive film) or the BM ribbons (3D nanoporous structure). In spite of the structural
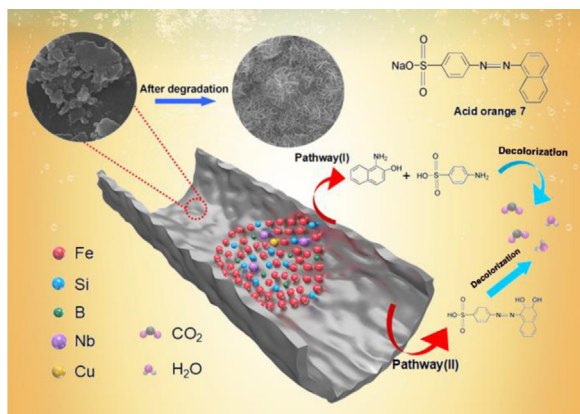
Fig. 11. Schematic diagram for the redox reaction process using BM ribbons.

relaxation and stress relief induced by annealing, the protrusions and corrugations allow the AN ribbons to show higher activity than the AQ ribbons because of the efficient mass transport on the loose surfaces. Besides, this result also implies that the stress gradient contributes to the formation of 3D nanoporous structure during degradation. The above analyses clarify that the highest degradation efficiency of BM ribbons comes from the joint effects of a loose surface and high deformation energy induced by ball milling.

3.4. Degradation pathways of AO7 solution during redox reaction using BM ribbons

The analysis of the products in the AO7 solution during reaction is performed using UHPLC-MS to elucidate the degradation pathways of AO7. The mass spectra of degradation products are shown in Fig. S4 (Supporting Information). Based on the m/z (mass-to-charge ratio) values, 16 intermediates are identified and listed in Table S2 (Supporting Information). For the simplicity of discussion, these intermediates are named as I1—I16. As no peak at m/z = 326.8 is detected, it is confirmed that AO7 is completely degraded [54] (sodium is dissociated from AO7 molecular structure in aqueous solution).

The donated electrons from Fe° of the BM ribbons can breakdown the AO7 molecules. And H^+ in the AO7 solution can accept electrons and react with water to form active group [H] [55], which also has ability to decompose AO7 molecules. Based on the above results, two possible pathways (pathway (I), pathway (II)) for the degradation of AO7 are presented, including azo bond cleavage and hydroxylation of benzene ring, as shown in Fig. 10.

In pathway (I), AO7 is degraded into the hydrazo derivatives due to cleavage of -N = N-, which leads to the formation of I1 and I2, but the intermediate I1 cannot be ascertained in ultra-violet spectra because it is very unstable and easily to be oxidized [56,57]. I1 is quickly oxidized to I4, which can produce intermediates I7, I8 and I9. The above three compounds are cleaved through ring-opening reactions, generating intermediate I12, which is then degraded to form I15. At the same time, I2 is rapidly oxidized to form I5, which is then desulfonated to become I10. The denitrification of I10 results in the formation of I13. And I13 could also be oxidized to I15. The above degradation pathways have been confirmed in several previous studies about the degradation of AO7 [56,58].

In pathway (II), AO7 is degraded into intermediate I3 (without breaking −NN)=− by the hydroxylation reaction. Afterwards, the I3 probably undergoes cleavage of the −NN =−and then partial oxidation on the benzene ring to form the ring-opening product I6. I6 is further oxidized to form I11, which then produces I2 and I14 through breakage and oxidation reaction. After that, the I2 possibly undergoes oxidation, desulfonation and denitrification on the

benzene ring to form I13. The I13 can be further degraded to I15 through degradation reactions. The product I14 undergoes deamination, resulting in the formation of I16. The degradation pathway (II) also has been confirmed in several previous studies about the degradation of AO7 [54,59]. Finally, these organic molecules (I15 and I16) are further decomposed and form CO_2, H_2O and inorganic ions [60–63].

Based on the above results and discussions, the schematic diagram for the redox reaction process using BM ribbons can be drawn in Fig. 11. After adding loose surface BM ribbons in the acidic AO7 solution, the stress gradient of BM ribbons contribute to the formation of 3D nanoporous structure during redox degradation. The loose surfaces and formed 3D nanoporous structures of BM ribbons provide mass and electron transport, which accelerates the oxidation of large AO7 molecules and breaks them down into small molecules.

4. Conclusion

This work assesses the effects of surface activation induced by ball milling on the dye degradation ability and reusability of FeSiBNbCu amorphous ribbons. The BM ribbons are able to decompose AO7 with far higher degradation efficiency and better reusability than the AQ ribbons. The higher degradation efficiency and better reusability of the BM ribbons are associated with the stored deformation energy and the uneven topography of the ribbon surface. The stress gradient produced of BM ribbons resulting from ball milling treatment contributes to the formation of 3D nanoporous structure during redox degradation. The BM ribbons have better degradation performance in acidic solutions. Moreover, two degradation pathways of AO7 are proposed, including azo bond cleavage and hydroxylation of benzene ring. This work provides a new method to simultaneously improve the dye degradation efficiency and reusability of amorphous ribbons.

Appendix A. Supplementary data

Supplementary material related to this article can be found, in the online version, at doi:https://doi.org/10.1016/j.jmst.2020.02.075.

References

[1] C. Suryanarayana, A. Inoue, Int. Mater. Rev. 58 (2013) 131–166.
[2] K.F. Yao, C.Q. Zhang,Appl. Phys. Lett. 90 (2007), 061901.
[3] F.B. Zhang, J.L. Wu, W. Jiang, Q.Z. Hu, B. Zhang, ACS Appl. Mater. Int. 9 (2017) 31340–31344.
[4] Z. Jia, X.G. Duan, P. Qin, W.C. Zhang, W.M. Wang, C. Yang, H.Q. Sun, S.B. Wang, L.C. Zhang,Adv. Funct. Mater. 27 (2017), 1702258.
[5] S.Q. Chen, G.N. Yang, S.T. Luo, S.J. Yin, J.L. Jia, Z. Li, S.H. Gao, Y. Shao, K.F. Yao, J. Mater. Chem. A 5 (2017) 14230–14240.
[6] Q.Q. Wang, M.X. Chen, P.H. Lin, Z.Q. Cui, C.L. Chu, B.L. Shen, J. Mater. Chem. A 6 (2018) 10686–10699.
[7] W.M. Yang, Q.Q. Wang, W.Y. Li, L. Xue, H.S. Liu, J. Zhou, J.Y. Mo, B.L. Shen, Mater. Des. 161 (2019) 136–146.
[8] Y. Tang, Y. Shao, N. Chen, X. Liu, S.Q. Chen, K.F. Yao, RSC Adv. 5 (2015) 34032–34039.
[9] L.C. Zhang, Z. Jia, F. Lyu, S.X. Liang, J. Lu,Prog. Mater. Sci. 105 (2019), 100576.
[10] L.C. Zhang, S.X. Liang, Chem-Asian J. 13 (2018) 3575–3592.
[11] C.Q. Zhang, Z.W. Zhu, H.F. Zhang, Z.Q. Hu, J. Environ, SciChina 24 (2012) 1021–1026.
[12] S.H. Xie, P. Huang, J.J. Kruzic, X.R. Zeng, H.X. Qian, Sci. Rep. 6 (2016) 21947.

[13] J.Q. Wang, Y.H. Liu, M.W. Chen, G.Q. Xie, D.V. Louzguine-Luzgin, A. Inoue, J.H. Perepezko, Adv. Funct. Mater. 22 (2012) 2567–2570.
[14] P.P. Wang, J.Q. Wang, J.T. Hou, W. Xu, X.M. Wang, G. Wang, Sci. China Phys. Mech. 60 (2017) 82–86.
[15] S.Q. Chen, N. Chen, M.T. Cheng, S.T. Luo, Y. Shao, K.F. Yao, Intermetallics 90 (2017) 30–35.
[16] S.X. Liang, Z. Jia, Y.J. Liu, W.C. Zhang, W.M. Wang, J. Lu, L.C. Zhang,Adv. Mater. 30 (2018), 1802764.
[17] Z. Jia, W.C. Zhang, W.M. Wang, D. Habibi, L.C. Zhang, Appl. Catal. B: Environ. 192 (2016) 46–56.
[18] J.Q. Wang, Y.H. Liu, M.W. Chen, D.V. Louzguine-luzgin, A. Inoue, J.H. Perepezko, Sci. Rep. 2 (2012) 418.
[19] S.Q. Chen, Y. Shao, M.T. Cheng, K.F. Yao, J. Non-Cryst. Solids 473 (2017) 74–78.
[20] Y.H. Sun, A. Concustell, A.L. Greer, Nat. Rev. Mater. 1 (2016) 16039.
[21] A.L. Greer, Y.H. Sun, Philos. Mag. Abingdon (Abingdon) 96 (2016) 1643–1663.
[22] M. Wakeda, J. Saida, J. Li, S. Ogata, Sci. Rep. 5 (2015) 10545.
[23] J. Pan, Y.X. Wang, Q. Guo, D. Zhang, A.L. Greer, Y. Li, Nat. Commun. 9 (2018) 560.
[24] W. Dmowski, Y. Yokoyama, A. Chuang, Y. Ren, M. Umemoto, K. Tsuchiya, A. Inoue, T. Egami, Acta Mater. 58 (2010) 429–438.
[25] C.C. Yang, X.F. Bian, J.F. Yang,Funct. Mater. Lett. 7 (2014), 1450028.
[26] B. Lin, X.F. Bian, P. Wang, G.P. Luo, Mater. Sci. Eng. B 177 (2012) 92–95.
[27] Z. Jia, J. Kang, W.C. Zhang, W.M. Wang, C. Yang, H. Sun, D. Habibi, L.C. Zhang, Appl. Catal. B-Environ. 204 (2017) 537–547.
[28] M. Tejedor, J.A. Garcia, J. Carrizo, L. Elbaile, J. Mater. Sci. 32 (1997) 2337–2340.
[29] M. Stylidi, D.I. Kondarides, X.E. Verykios, Appl. Catal. B: Environ. 47 (2004) 189–201.
[30] F. Miao, Q.Q. Wang, Q.S. Zeng, L. Hou, T. Liang, Z.Q. Cui, B.L. Shen, J. Mater. Sci. Technol. 38 (2020) 107–118.
[31] S.X. Liang, Z. Jia, W.C. Zhang, X.F. Li, W.M. Wang, H.C. Lin, L.C. Zhang, Appl. Catal. B: Environ. 221 (2018) 108–118.
[32] S.X. Liang, X.Q. Wang, W.C. Zhang, Y.J. Liu, W.M. Wang, L.C. Zhang,Appl. Mater. Today 19 (2020), 100543.
[33] S.X. Liang, W.C. Zhang, L.N. Zhang, W.M. Wang, L.C. Zhang,Sustain. Mater. Technol. 22 (2019), e00126.
[34] Z. Jia, Q. Wang, L. Sun, Q. Wang, L.C. Zhang, G. Wu, J.H. Luan, Z.B. Jiao, A.D. Wang, S.X. Liang, M. Gu, J. Lu,Adv. Funct. Mater. 29 (2019), 1807857.
[35] S.V. Ketov, Y.H. Sun, S. Nachum, Z. Lu, A. Checchi, A.R. Beraldin, H.Y. Bai, W.H. Wang, D.V. Louzguine-Luzgin, M.A. Carpenter, A.L. Greer, Nature 524 (2015) 200–203.
[36] W.L. Song, X.H. Meng, Y. Wu, D. Cao, H. Wang, X.J. Liu, X.Z. Wang, Z.P. Lu, Sci. Bull. (Beijing) 63 (2018) 840–844.
[37] J. Pan, Q. Chen, L. Liu, Y. Li, Acta Mater. 59 (2011) 5146–5158.
[38] J. Qiang, K. Tsuchiya, J. Alloys. Compd. 712 (2017) 250–255.
[39] A. Slipenyuk, J. Eckert, Scr. Mater. 50 (2004) 39–44.
[40] L.Y. Guo, X. Wang, K.C. Shen, K.B. Kim, S. Lan, X.L. Wang, W.M. Wang, J. Mater. Sci. Technol. 35 (2019) 118–126.
[41] H.S. Chen, Appl. Phys. Lett. 29 (1976) 328–330.
[42] J.D. Livingston, W.G. Morris, J. Appl. Phys. 57 (1985) 3555–3559.
[43] J.D. Livingston, Phys. Stat. Sol. 56 (1979) 637–645.
[44] M.E. Hawley, G.W. Brown, D.J. Markiewicz, F. Spaepen, E.P. Barth, J. Magn. Magn. Mater. 190 (1998) 89–97.
[45] L.Q. Shen, P. Luo, Y.C. Hu, H.Y. Bai, Y.H. Sun, B.A. Sun, Y.H. Liu, W.H. Wang, Nat. Commun. 9 (2018) 4414.
[46] S.X. Liang, Z. Jia, W.C. Zhang, W.M. Wang, L.C. Zhang, Mater. Des. 119 (2017) 244–253.
[47] Q.Q. Wang, L. Yun, M.X. Chen, D.D. Xu, Z.Q. Cui, Q.S. Zeng, P.H. Lin, C.L. Chu, B.L. Shen, ACS Appl. Nano Mater. 2 (2019) 214–227.
[48] K. Zhang, L.L. Zhang, X.S. Zhao, J.S. Wu, Chem. Mater. 22 (2010) 1392–1401.
[49] S. Narayanasamy, J. Jayaprakash, Chem. Eng. J. 343 (2018) 258–269.
[50] Q.Y. Niu, K.Z. Gao, Q.H. Tang, L.Z. Wang, L.F. Han, H. Fang, Y. Zhang, S.W. Wang, L.X. Wang, Carbon 123 (2017) 290–298.
[51] Y.J. Kim, I.Y. Jang, K.C. Park, Y.C. Jung, T. Oka, S. Iinou, Y. Komori, T. Kozutsumi, T. Hashiba, Y.A. Kim, M. Endo, Electrochim. Acta 55 (2010) 5624–5628.
[52] J.J. Wang, Y.H. Ma, S. Feng, J.D. Wang, J. Coat. Technol. Res. 16 (2019) 827–834.
[53] G. Sahoo, R. Balasubramaniam, Corros. Sci. 50 (2008) 131–143.
[54] J.H. Shen, J.J. Horng, Y.S. Wang, Y.R. Zeng, Chemosphere 182 (2017) 364–372.
[55] L. Zhang, X. Gao, Z.X. Zhang, M.B. Zhang, Y.Q. Cheng, J.X. Su, Sci. Rep. 6 (2016) 31797.
[56] G.X. Quan, L.J. Kong, Y.Q. Lan, B. Gao, Appl. Clay Sci. 152 (2018) 173–182.
[57] G.X. Quan, W.J. Sun, J.L. Yan, Y.Q. Lan, Water Air Soil Pollut. Focus. 225 (2014) 2195–2205.
[58] W.E. Thung, S.A. Ong, L.N. Ho, Y.S. Wong, F. Ridwan, H.K. Lehl, Y.L. Oon, Y.S. Oon, Chem. Eng. J. 336 (2018) 397–405.
[59] P. Bansal, D. Singh, D. Sud, Sep. Purif. Technol. 72 (2010) 357–365.
[60] C.X. Zhang, Y.B. Sun, Z.Q. Yu, G.Y. Zhang, J.W. Feng, Chemosphere 191 (2018) 527–536.
[61] Y. Xu, L. Lin, Y.K. Li, H. Zhang, Sci. Total Environ. 609 (2017) 644–654.
[62] S.D. Yan, W.H. Xiong, S.Y. Xing, Y.Q. Shao, R. Guo, H. Zhang, Sci. Total Environ. 599 (2017) 1181–1190.
[63] T.C. Wang, G.Z. Qu, J.Y. Ren, Q.H. Sun, D.L. Liang, S.B. Hu, J. Hazard. Mater. 302 (2016) 65–71.